Journal of Alloys and Compounds 773 (2019) 401–412

Contents lists available at ScienceDirect

Journal of Alloys and Compounds

journal homepage: http://www.elsevier.com/locate/jalcom

Oxygen-driven impurities scavenging before solidification of Fe-based metallic glasses

Weiming Yang [a], Qianqian Wang [b, 1], Haibo Ling [c], Haishun Liu [a, *], Lin Xue [b], Yezeng He [a], Qiang Li [c], Baolong Shen [b, **]

[a] School of Mechanics and Civil Engineering, Institute of Massive Amorphous Metal Science, China University of Mining and Technology, Xuzhou, 221116, People's Republic of China
[b] School of Materials Science and Engineering, Southeast University, Nanjing, 211189, People's Republic of China
[c] School of Physics Science and Technology, Xinjiang University, Urumqi, Xinjiang, 830046, People's Republic of China

ARTICLE INFO

Article history:
Received 11 July 2018
Received in revised form
17 September 2018
Accepted 19 September 2018
Available online 20 September 2018

Keywords:
Fe-based metallic glasses
Oxygen and impurities
Impurity-scavenger

ABSTRACT

Oxygen and impurities are basically unavoidable during the manufacturing of Fe-based metallic glasses, frequently impeding the products' performance and greatly increasing the processing cost. Until now, how oxygen affects the glass-forming ability remains controversial, and eliminating the adverse effects of oxygen and impurities is still a huge challenge. Here we discover a new force of oxide inclusion flotation that drives the occurrence of purification, by blowing oxygen into the Fe-based melts, which help to mix the melts well to accelerate the oxidization and elimination of impurities from commercial raw materials. The synergistic reaction of oxygen and impurities not only improves the glass forming ability, magnetic and mechanical properties of the products, but also makes the stringent processing requirements, e.g. high-purity starting materials and/or high-purity argon, unnecessary. This study uncovers the mystery of oxygen in the glass formation, extends the innovation of fabrication process and highlights a significant technological breakthrough to reduce industrial production cost of Fe-based metallic glasses.

1. Introduction

The materials purity and the vacuum degree in the manufactories are not as desirable as in the laboratories, restraining the large-scale industrialization of research findings, among which Fe-based metallic glasses (FMGs) are typical examples. FMGs have attracted great research development interests [1] ever since their first synthesis in 1967 [2] because of their superior soft magnetic [3], mechanical and chemical [4,5] properties [6], as well as their relatively low cost of manufacture [7]. Especially, many large-sized FMGs have been developed in the laboratories since the discovery of bulk FMGs in 1995 [8], and they were considered to possess promising applications as structural and surface coating materials [9,10]. However, the actual number of FMGs suitable for the commercial production is quite limited and their applications, particularly as structural materials, are rarely reported. The stringent processing requirements for the formation of FMGs, i.e. under high vacuum and using high-purity starting materials, aiming to reduce the detrimental effects of oxygen and the inclusions (e. g. Al, Si, Cr, S and their oxides), increase the production cost and impede the industrialization of these alloys.

There is no debate about the adverse effect of the inclusions as their alloying assists heterogeneous nucleation and deteriorates the chemical, mechanical and soft magnetic properties of FMGs [11,12]. Nevertheless, the role of oxygen in metallic glasses preparation has remained controversial for more than 20 years [13–16]. W. L. Johnson et al. found oxygen detrimental to glass formation as it induced formation of harmful oxides and/or metastable phases which act as heterogeneous nucleation sites [17]. J. Eckert et al. suggested that inclusions of oxygen impurities changed the crystallization process from single to multiple stages and then decreased the supercooled liquid region [18]. On the contrary, D. J. Sordelet et al. revealed that a critical level of oxygen could promote glass formation [19–22]. Moreover, the oxygen concentration varies significantly in different samples even of the similar

* Corresponding author.
** Corresponding author.
E-mail addresses: liuhaishun@126.com (H. Liu), blshen@seu.edu.cn (B. Shen).
[1] Contributes equally with the first author.

https://doi.org/10.1016/j.jallcom.2018.09.242
0925-8388/

compositions [23], e.g. the oxygen concentration measured by V. Ponnambalam et al. [24], as low as 50 ppm or less in $Fe_{48}Cr_{15}Mo_{14}Y_2C_{15}B_6$ glassy alloy, which is about 20–50 times lower than that in similar glassy alloys synthesized by Z.P. Lu et al. [25]. These debates indicate that a physical understanding of the mechanisms of oxygen alloying in FMGs is still unsettled. As the oxygen and inclusions alloying are basically unavoidable during the large-scale industrial processing, it is vital to understand and overcome its adverse effect in the glass formation process, in order to produce the similar (or better) samples in commercial production as in the laboratories and facilitate the applications of FMGs tremendously.

Recently, it was found that oxygen-scavenger elements, e.g. Al, Y, function well in decreasing the oxygen concentration to improve the manufacturability in the glass matrix via the formation of oxides [25,26]. From the other point of view, oxygen is also capable to trap these scavenger elements and eliminate their impact to the matrix [27]. The FMGs also can be successfully synthesized in air [28,29], even in oxygen [22]. These standpoints enlighten us a new possibly-effective approach to reduce the adverse impact of the impurities for the industrial production of FMGs, by blowing a suitable amount of “impurity-scavenger"—oxygen in the metallic melts. This will definitely reduce the industrial production cost of FMGs, as neither high-purity starting materials nor high vacuum degree is necessary for this approach.

To verify the above idea, taking typical Fe-P-C ternary system as an example, we built a torch-heated transparent quartz tube system and blew oxygen/argon during the melting process to prepare FMGs. The relative low affinity for oxygen of P and C during melting, as well as the simplicity of the ternary system, allow us to investigate most of the impurity elements without obscure. The transparent quartz tubes enable us to observe the experimental phenomenon easily and control the gas flow precisely. Fluxing treatment was performed on the alloys prior to the melting process to eliminate the oxygen dissolved in the starting materials. We found that the oxygen blew during the melting and the casting process function as the “impurity-scavenger", and provide a new force of oxide inclusion flotation that drives the occurrence of purification, which assists the glass formation and promotes the magnetic and mechanical properties of bulk FMGs. This finding not only uncovers the mystery of oxygen in the formation process of FMGs, but also gives a useful guideline in the innovation of fabrication process for reducing their industrial production cost.

2. Methods

2.1. Materials and preparation

Mother alloy ingots with nominal compositions of $Fe_{80}P_{13}C_7$ (at. %) were prepared by employing commercial raw materials: Fe-P, Fe-C alloys and iron powder (99.8 wt % Fe, other constituents including Al, Cr and their oxides). Wet chemical composition analysis results of the industrial grade raw materials Fe-P and Fe-C are shown in Table 1. The alloy ingots were fluxed with a fluxing agent composed of B_2O_3 and CaO (mass ratio of 3:1) at 1500 K for several hours under a vacuum of ~10 Pa, to decrease the initial amount of oxygen dissolved in the melts.

After fluxing treatment, the alloy was transferred into the transparent quartz tube system, which consists of two tubes with different diameters connecting to each other. The typical dimensions of the larger tubes are 5–10 cm in length, with inner/outer diameter being 11/13 mm. The smaller tubes are 5–10 cm in length, 0.1–0.2 mm in wall thickness and 1–2 mm in inner diameter, respectively. The tube system was connected to a mechanical pump and evacuated to ~5×10^{-3} Torr first, and then blew with corresponding high purity (below 1 atm) Ar or O_2 gas continuously. The ingot was melted using a torch and heated the melt to ~1450 K by holding for 5, 10 and 15s. To achieve rapid quenching, the melt was then pushed into the smaller quartz tube. Subsequently, the tube system was moved out of the furnace and quenched in cold water (room temperature) for several minutes. The cylindrical alloy samples with diameters of 1.0–2.0 mm and lengths of a few centimeters were obtained.

2.2. Structure characterization

The nature of samples was ascertained by X-ray diffraction (XRD) (D8 Advance) with Cu Kα radiation, differential scanning calorimetry (DSC) (NETZSCH DSC-404) with a heating rate of 0.33 K/s, and high-resolution transmission electron microscopy (HRTEM) (Tecnai F20). The as-quenched glassy rods were cut in half along the longitudinal axis, polished and etched by a 5% HNO_3-C_2H_5OH solution, the inclusions inside the samples were observed and identified by optical microscope, scanning electron microscopy (SEM) and energy dispersive spectroscopy (EDS).

The binding states of glassy rods were evaluated by X-ray photoelectron spectroscopy (XPS) using a Kratos AXIS ULTRA^{DLD} instrument with a monochromic Al K_α X-ray source ($h\nu = 1486.6$ eV). The power was 120 W and the X-ray spot size was set to be 700 × 300 μm. The pass energy of the XPS analyzer was set at 20 eV. The base pressure of the analysis chamber was better than 5×10^{-9} Torr. All spectra were calibrated using the binding energy (BE) of C 1s (284.8 eV) as a reference, ultraviolet source (He I 21.2 eV and He II 40.8 eV) and etching condition (beam energy 2.0 kV, extractor current 100 μA, raster size 4 mm).

Needle-shape specimens for atom probe tomography (APT) were fabricated by a lift-out method in a FEI Nova™ 200 Nanolab™ focused ion beam instrument. The APT analyses were performed in a Cameca Instruments LEAP 4000X HR in either voltage or laser ($\lambda = 400$ nm, 100 kHz pulse repetition rate) modes.

2.3. Performance measurement

The specimens for compression test were cut out from the as-quenched rods, and each end was polished to make it parallel to each other prior to the compression test. The mechanical behavior of at least 10 specimens for each sample with a diameter of 1.0 mm and an aspect ratio of 2:1 was examined by uniaxial compression using an Instron testing machine at room temperature, and the strain rate was 5×10^{-4} s^{-1}. The tests were carried out in a constant-crosshead-displacement-rate control manner.

Magnetic properties of saturation magnetization (M_S) were measured on the glassy rods at room temperature with a vibrating

Table 1
The main chemical composition of Fe-P and Fe-C commercial raw materials.

Materials (wt %)	Fe	Si	Cr	P	Al	C	S	Others
Fe	99.800	0.050	0.084	0.012	0.010	0.008	0.006	0.030
Fe-P	73.161	0.009	–	26.803	–	0.015	0.012	–
Fe-C	94.351	1.559	–	0.106	–	3.984	–	–

sample magnetometer (VSM) under an applied field of 800 kA/m.

2.4. First-principles calculations

First-principles calculations were used to study the adsorption behavior of the α-Al_2O_3 based on density functional theory within the generalized-gradient approximation and with the Perdew-Burke-Ernzerhof functional and ultrasoft pseudo potential. The Brillouin zone was sampled with $(5 \times 5 \times 1)$ k points of a Monkhorst-Pack grid. The energy cutoff for the plane-wave expansion of the eigenfunctions was set to 400 eV. To simulate the adsorption on the surface of α-Al_2O_3, we constructed a slab model with a 15 Å vacuum depth along the [0001] direction and a surface unit cell with a 2×2 dimension. For all surface calculations, the bottom three layers were kept frozen and the other layers were allowed to relax. The structure optimization was performed until the Hellmann-Feynman force on each atom less than 0.02 eV/Å. The convergence of the total energy is considered to be achieved until two iterated steps with energy difference is less than 10^{-5} eV. The adsorption energy is calculated as $E_{ad} = E(aa/Al_2O_3)$-$E(Al_2O_3)$-$E(aa)$. In the equation, $E(aa/Al_2O_3)$ and $E(Al_2O_3)$ are the total energies of the supports with and without the adsorption atoms, respectively, while $E(aa)$ is the total energy of the adsorption atoms.

3. Results

3.1. Comprehensive properties of glassy rods prepared in argon and in oxygen

To clarify the effect of oxygen in the preparation of FMGs, we prepared $Fe_{80}P_{13}C_7$ glassy rods using commercial raw materials under high purity argon (Ar-rod) and oxygen (O_2-rod) atmosphere respectively (see Methods part for sample preparation details), and analyzed their glass forming ability (GFA), magnetic and mechanical properties subsequently. The critical diameter of the Ar-rod is 1.0 mm, while 2.0 mm glassy rods are successfully obtained by blowing high purity oxygen during heating, referring to higher GFA, as X-ray diffraction (XRD) patterns show in Fig. 1 (a). The DSC analyses of the obtained glassy rods are presented in Fig. 1 (b). The Ar-rod exhibits a single sharp exothermic peak, suggesting a simultaneous formation of the different crystalline phases. Interestingly, the crystallization behavior of the O_2-rod changes from single to a double-step process. Further study of the splitting crystallization peaks is presented in the discussion part in this work. Magnetic properties analyses of as-cast glassy rods were carried out via VSM as shown in Fig. 1 (c). We find that Ar-rod and O_2-rod display similar M-H loop shape and exhibit similar values of M_S, only that the M_S of O_2-rod sample is slightly larger than that of Ar-rod. Typical mechanical properties of engineering fracture strength and compressive plastic strain of Ar-rod and O_2-rod samples also have been compared, as shown in Fig. 1 (d). Although the yield strength of $Fe_{80}P_{13}C_7$ glassy alloys prepared in argon and oxygen are similar, about 3.4 GPa, the plastic strain increases visibly from 1% for Ar-rod to 3% for O_2-rod.

3.2. Structure and composition analyses of glassy rods prepared in argon and in oxygen

SEM analyses of the surface and interior of Ar-rod and O_2-rod are presented in Fig. 2. The surface morphology of the two samples

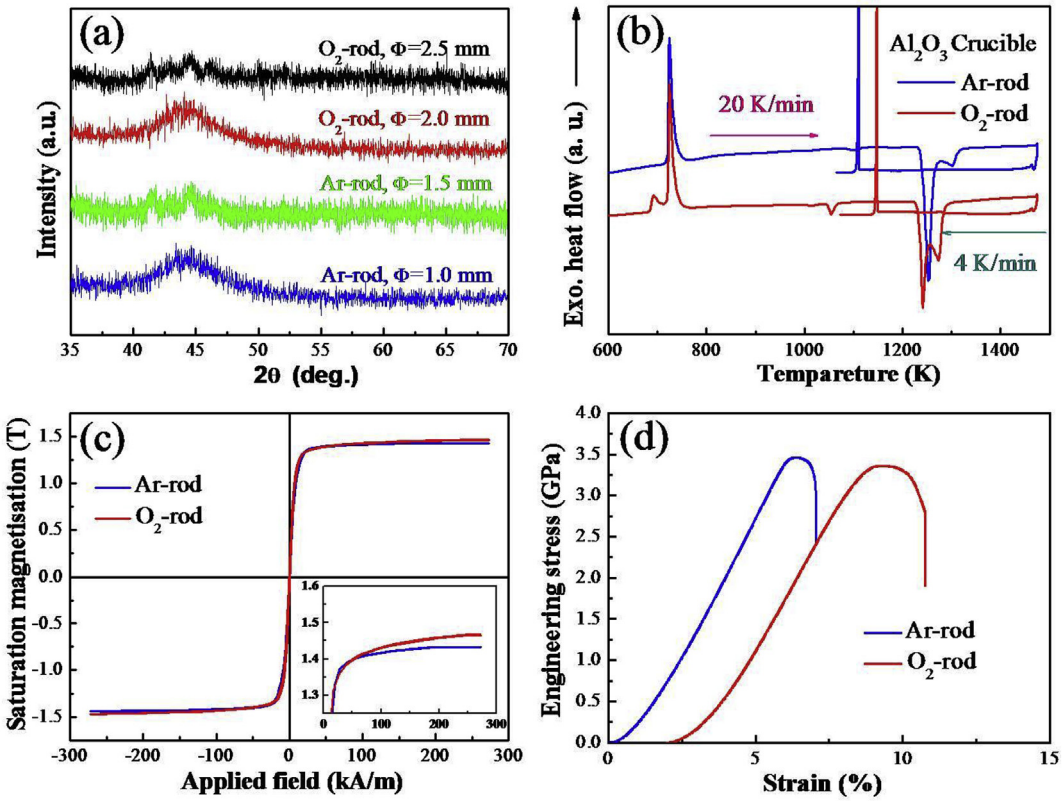

Fig. 1. (a) XRD patterns of $Fe_{80}P_{13}C_7$ glassy rods with various diameters prepared using commercial raw materials under high purity argon (Ar-rod) and oxygen (O_2-rod) atmosphere, respectively. (b) DSC curves of Ar-rod and O_2-rod with a diameter of 1.0 mm. (c) Hysteresis M-H loops of Ar-rod and O_2-rod with a diameter of 1.0 mm. (d) Mechanical properties of Ar-rod and O_2-rod with a diameter of 1.0 mm.

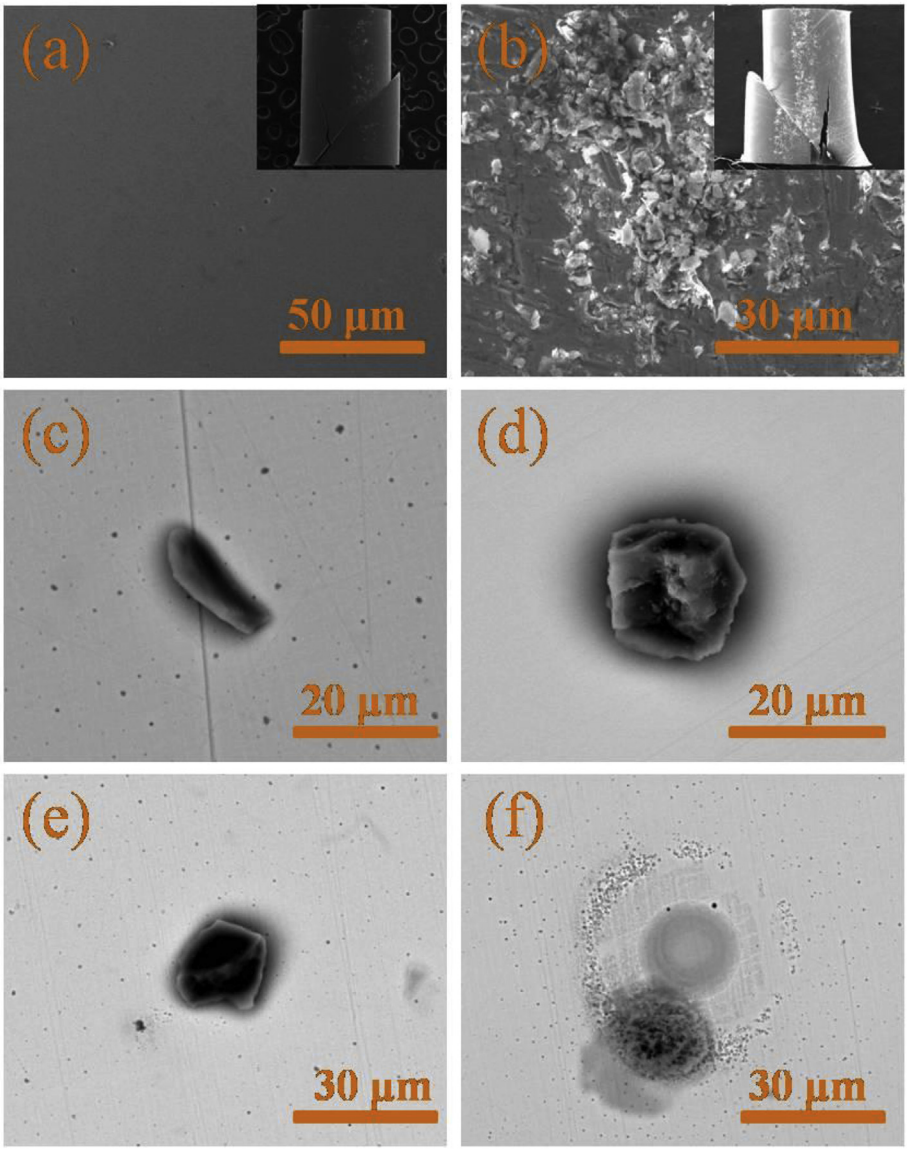

Fig. 2. (a) and (b) SEM images of the surfaces of the Ar-rod and the O_2-rod, respectively, the insets show their macroscopic compression samples before breaking. (c) and (e) SEM images of the interiors of the Ar-rod. (d) and (f) SEM images of the interiors of the O_2-rod.

subjected to compression test (prior to failure) are completely different. Nearly no inclusions are observed on the surface of the Ar-rod (Fig. 2 (a)), while a large amount of inclusions accumulate on the surface of the O_2-rod (Fig. 2 (b)). These inclusions are primarily composed of Al_2O_3, Cr_2O_3, CaS, SiO_2 *etc.* (see Fig. 3 and Table 2) and minor amounts of bubble-like cavities. A special feature also has been regularly observed on the O_2-rod surface, on which the majority of inclusions tend to combine to form the large oxide-based inclusions.

The special interior features of these two kinds of glassy rods are presented in Fig. 2 (c)~(f). There are many small spherical inclusions (<1 μm), together with seldom large inclusions, embedded randomly in the whole Ar-rod samples as shown in Fig. 2 (c) and (e). However, nearly no inclusions are observed in most scanned regions in the O_2-rod samples, except that seldom appears single large spherical inclusion without any other feature around as shown in Fig. 2 (d). Luckily, the formation process of these large but rare inclusions in O_2-rod is captured under SEM, lots of embryos of small inclusions colliding with each other and coalescing into bigger ones, as shown in Fig. 2 (f). Meanwhile, cavities are also found in some scanned regions under SEM (EDS results see Fig. 4). The inner wall of the cavities is rather smooth without any dendritic feature (Fig. 5), which means that gas should exist in the formation process of the cavities.

Wet chemical composition analyses were performed on the commercial raw materials used in this work, presenting trace amount of Si, Cr, Al, S and other impurities in the alloys, as shown in Table 1. To eliminate the influence of oxygen coming from the raw materials, we utilized melt fluxing method on the ingots prior to carrying out the experiments in the tube system. The overall oxygen concentration of flux-melted alloys is usually below 2 ppm [30,31]. To trace the distribution of these impurities and oxygen, EDS line scanning were performed on the inclusions and the glass matrix both in Ar-rod and O_2-rod. Representative EDS line scanning result is shown in Fig. 6, uncovering the existence of Ca and S in the inclusion. S comes from the impurities of the starting materials, while Ca coming from the fluxing treatment process. Impurity elements distribute in different inclusions, e.g. Si, Cr or Al, are not

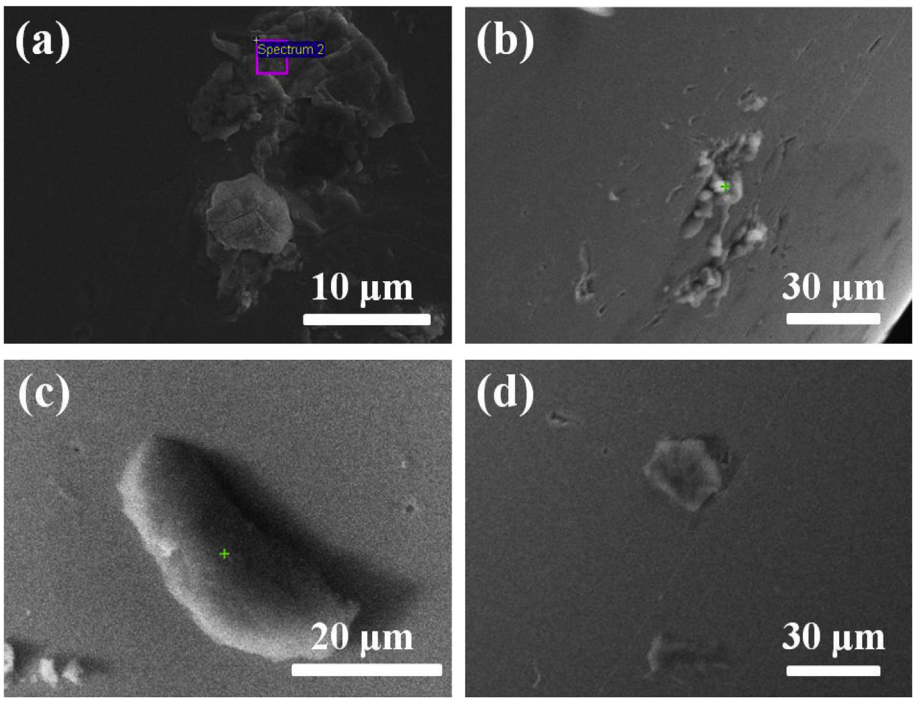

Fig. 3. Morphologies of the represented inclusions on the surface of O_2-rods.

Table 2
The composition results (wt.%) of the inclusions in Fig. 3 analyzed by EDS.

	Fe	P	C	O	Al	Cr	Si	S	Ca	other
Fig. 3 (a)	54.64	3.35	1.35	20.65	13.87	6.13	–	–	–	–
Fig. 3 (b)	4.68	0.48	66.03	28.43	0.09	–	–	0.29	–	–
Fig. 3 (c)	23.20	1.40	51.49	19.59	0.14	–	–	1.27	0.16	4.46
Fig. 3 (d)	69.20	15.76	6.27	8.65	0.05	–	0.02	0.02	0.03	–

detected in the inclusions in Fig. 6 but present in other inclusions (Fig. 3, Table 2). The oxygen distribution is also obtained via EDS line scanning. Surprisingly, no matter what kind of airs, oxygen or argon are blown during the preparation process, the oxygen concentration in the glass matrix is always very low, which is confirmed by 3DAP results (Fig. 7), while it is much higher in the inclusions. In contrast, the concentration of Fe and P in the

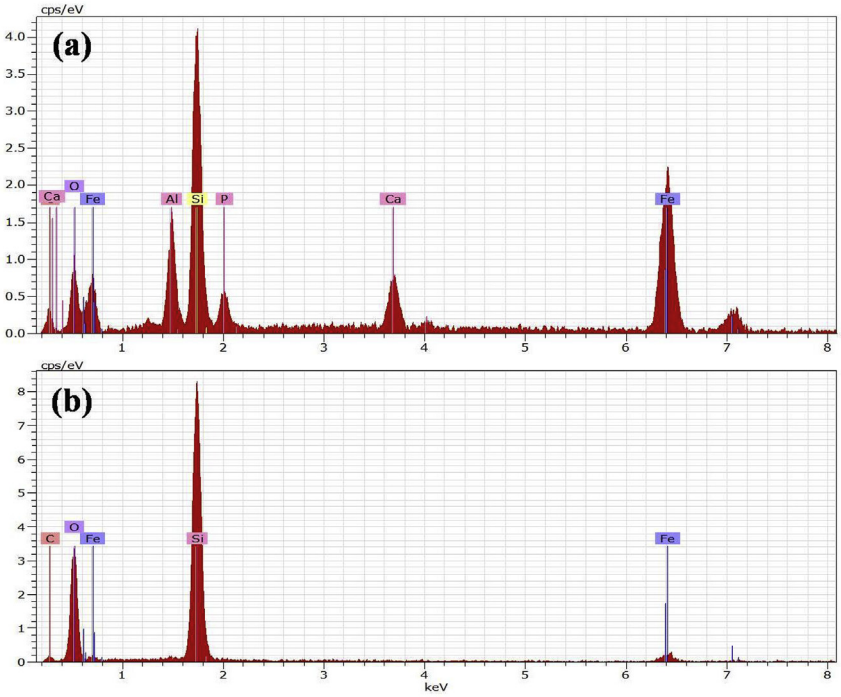

Fig. 4. The coexistence of alumina, silicides and other oxides in the interior of the samples prepared in argon. (a) The EDS result for inclusions in Fig. 2 (c); (b) The EDS result for inclusions in Fig. 2 (e).

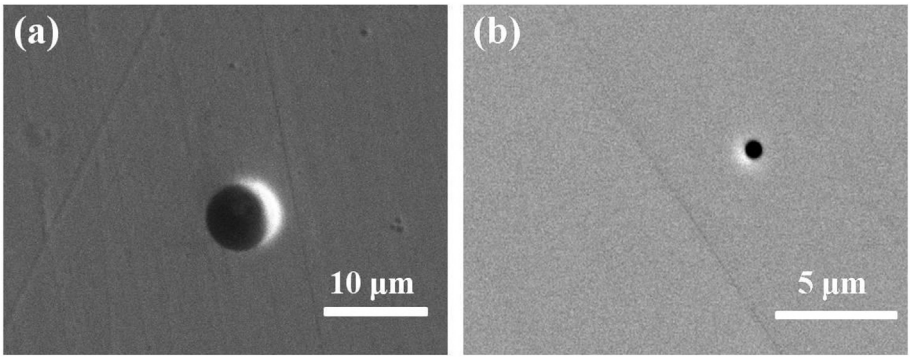

Fig. 5. The bubble-like cavities in the interior of the O_2-rod. (a) and (b) show two typical morphologies of bubble-like cavities at different positions.

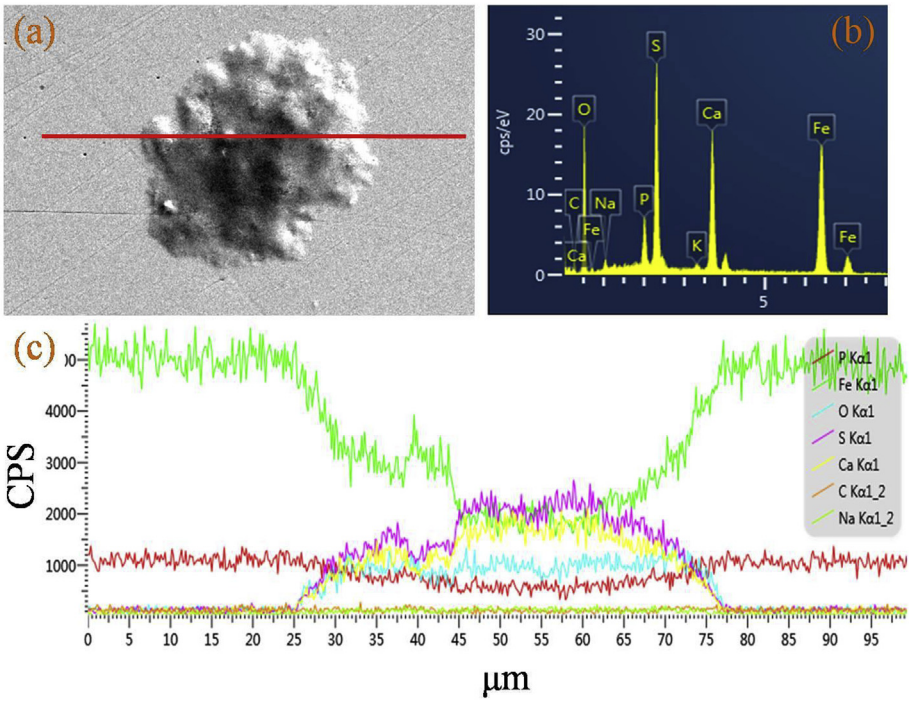

Fig. 6. (a) A typical inclusion in the glassy samples. (b) The EDS result of the inclusion in (a). (c) The composition profile of the selected red line in (a) using the EDS line scan. (For interpretation of the references to colour in this figure legend, the reader is referred to the Web version of this article.)

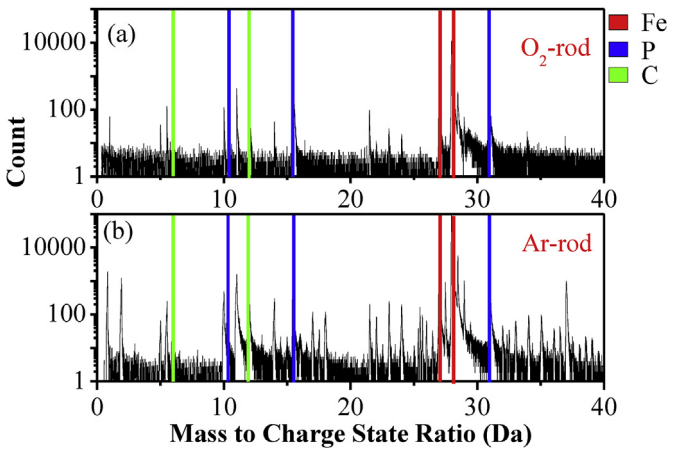

Fig. 7. Atom probe analysis of (a) O_2-rod and (b) Ar-rod. The concentration of oxygen is too low to be detected by Mass spectrum analysis.

inclusion is lower than that in the glass matrix. It clearly reveals that the oxygen is only absorbed and dissolved homogeneously into the inclusions. This result also suggests that oxygen is not introduced into the glass matrix by blowing oxygen. Iron-rich melts can dissolve large amounts of oxygen. The oxygen in ferro-alloys mainly exists in oxides form because of its limited solubility in ferro-alloys. On cooling this melt, the dissolved oxygen will precipitate into crystalline oxide inclusions that may become potential hetero nucleates.

In order to obtain further microstructure information of the Ar-rod and O_2-rod, we applied XPS to both samples over a wide binding energy region to measure the peaks of Fe-2p, P-2p, C-1s, Al-2p, S-2s, Cr-2p, Si-2p, O-1s, etc. There is no difference of the XPS spectra of Fe-2p, P-2p and C-1s measured for all specimens (2–4 nm detection depth). The Fe-2p spectra of both Ar-rod and O_2-rod display the characteristic features for metallic states and the P-2p and C-1s spectra display the characteristic features for non-oxidized states (Data not shown). For Ar-rod samples, the S existence is well confirmed using XPS in Fig. 8 (a). The S-2p spectrum

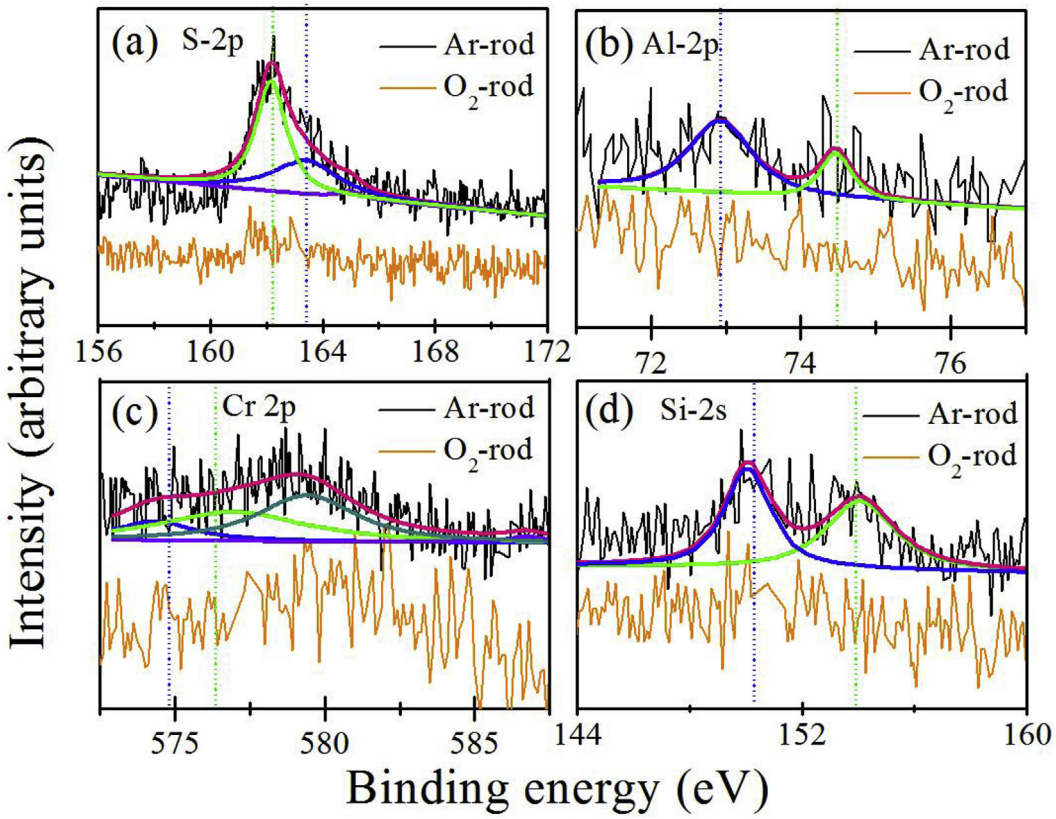

Fig. 8. (a), (b), (c) and (d) the XPS data of Al-2p, S-2p, Cr-2p and Si-2s in the Ar-rod and O_2-rod, respectively. (Blue line represents elementary state, green line represents ion state, red line represents the sum of elementary and ion states). (For interpretation of the references to colour in this figure legend, the reader is referred to the Web version of this article.)

consists of one set of 2p3/2 (164.0 eV) and 2p1/2 (162.5 eV) peaks. The peak at 162.1–162.5 eV is assigned to S-2p electrons of S^{2-} ions. Although the integrated intensities of Al, Cr, and Si peaks are small in the Ar-rod, their existence can still be detected. The peak at 72.9–73.1 eV corresponds to the metallic state (Al^0), while the Al-2p peak at 74.3–74.5 eV corresponds to the Al^{3+} state appear for Ar-rod in Fig. 8 (b). The peak at 578–581 eV corresponds to Cr^0 and Cr^{3+} in Fig. 8 (c), while the peaks at 149–152 eV and 154 eV corresponds to Si and Si^{4+} in Fig. 8 (d) in Ar-rod, respectively. The distinct chemical shifts towards higher binding energies were observed due to the additional contributions from Al_2O_3, CaS, *etc.* inclusions in alloy prepared by blowing Ar. In contrast, from the XPS analyses we reveal that the peaks of Al, S, Cr and Si are very slight or disappear if the samples were prepared by blowing oxygen. These results imply that the role of oxygen seems to be the scavenger of inclusions.

3.3. Pesudo-in situ observation of the inclusions formation process in melts

To elaborate the effects of oxygen in the formation of inclusions in the production of FMGs, we analyzed the microstructure transformation inside the obtained rods via the holding time of the melts in argon and oxygen atmosphere respectively. Before quenching the tube system in cold water, we held the melts in the tube system in an oven at ~1450 K for 5, 10 and 15 s, blowing argon and oxygen, respectively. The microstructure of these melts was then "frozen" in the obtained rods by quenching, providing pseudo-in situ observation of the inclusion formation process. Real-time pictures of these melts after holding were taken and presented in Fig. 9. Some melts and inclusions splash on the inner wall of the transparent tubes, and the whole melts becomes stable after 10s with oxygen blowing, while all the tubes with argon blowing are very clean. The obtained rods after quenching were cut and polished to be analyzed under optical microscope. Cross sections of O_2-rods with different holding time are presented in Fig. 10 (a)~(c). When blowing oxygen during the heating process, with the increasing holding time, the size of the inclusions increases but the amount of the inclusions decreases significantly and finally disappear. A large amount of small inclusions is trapped in the O_2-rod by heating the melt for 5 s; the amount of inclusions is significantly reduced despite the existence of some relatively large inclusions formed from the accumulation of the small inclusions by heating the melt for 10 s; Surprisingly, by heating the melts for 15 s, no inclusion is visible on the cross section of the O_2-rod. These results reveal that the gas atmosphere has a primary effect on inclusions cleanliness. When blowing argon during the heating process, neither the size nor the amount of inclusions changes much (Fig. 10 (d)-(f)). Inclusions with diameters in the range of 0.5–5 μm are trapped in the Ar-rods when holding the melt for 5s, 10s or 15s. On the other hand, DSC analysis of obtained Ar-rod and O_2-rod with different holding time reveals that, longer heating time leads to the splitting crystallization peaks in the O_2-rods (Fig. 11). This result implies that the inclusions change the crystallization process of O_2-rods.

4. Discussion

Among all the efforts for GFA improvement, employing oxygen-scavenger in the glass matrix has been proved to be an effective method [15,26]. Some elements have stronger affinity for oxygen than other elements and thermodynamically more favored to react with oxygen to alleviate the oxygen impurity impact in the system,

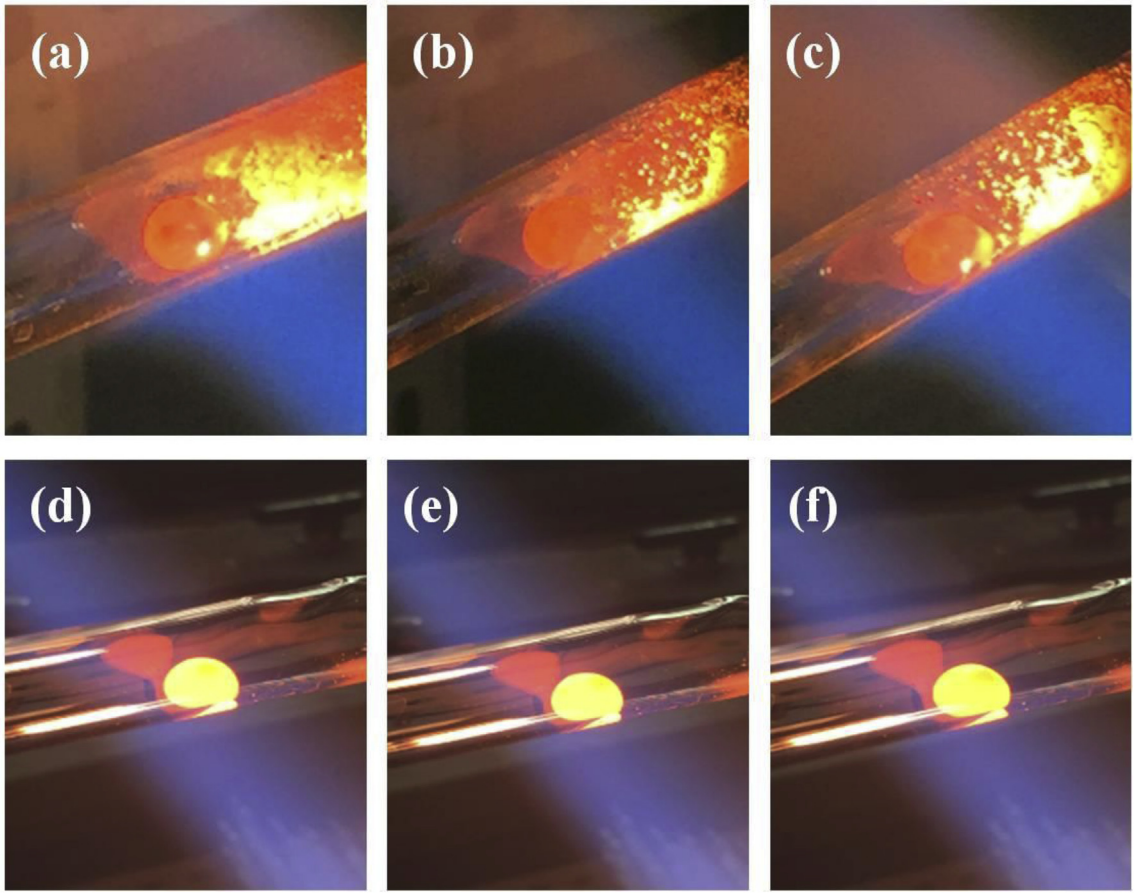

Fig. 9. (a)~(c) The optical graphs for the $Fe_{80}P_{13}C_7$ melts under high-purity oxygen atmosphere at different continuous heating time, 5s, 10s and 15s. (d)–(f) The optical graphs for the $Fe_{80}P_{13}C_7$ melts before cooling in a quartz tube under high-purity argon atmosphere at different continuous heating time5s, 10s and 15s.

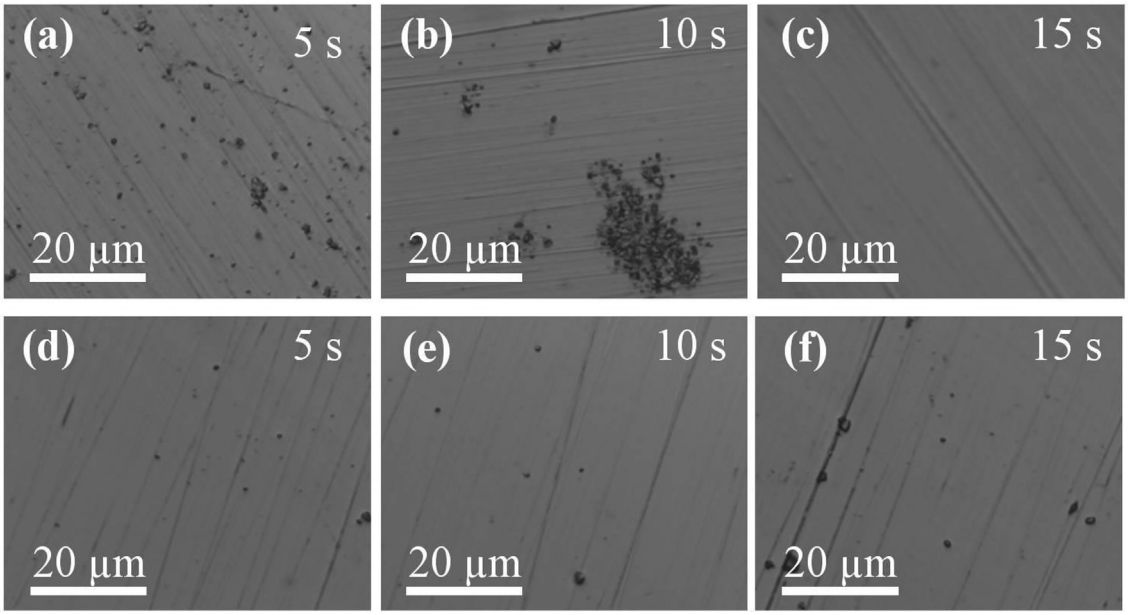

Fig. 10. Optical microscopy analyses of obtained O_2-rods and Ar-rods with different melt-state: Blowing oxygen and holding the melt for (a) 5s, (b) 10s and (c) 15s; Blowing Argon and holding the melt for (d) 5s, (e) 10s and (f) 15s.

so they are called “oxygen-scavenger". Minor addition of the oxygen-scavenger will improve the GFA of the matrix [25]. Oxygen-scavenger elements, e.g. Y, Al, Ti, function well in decreasing the oxygen concentration in the glass matrix. From another point of

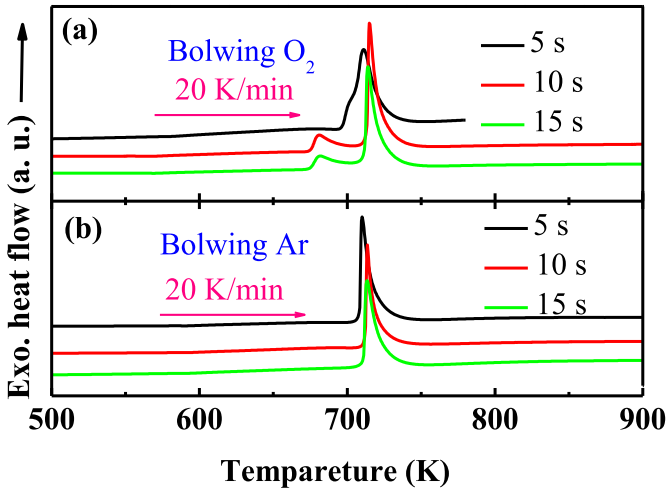

Fig. 11. DSC curves of (a) O_2-rod and (b) Ar-rod with a diameter of 1.0 mm from different holding times.

view, oxygen is also capable to trap these scavenger elements and eliminate their impact to the matrix [32]. In fact, the inclusions (e. g. Al, Ti, Y and their oxides) sometimes are brought into the alloy casually as the impurity elements due to the low purity of commercial starting materials. In this case, the oxygen should be referred as the "impurity-scavenger" in the glass matrix. In addition, compared with the traditional melt spinning process under vacuum, blowing oxygen input dynamic force to the melt, tremendously increase the mixing movement of the melt and the collision opportunity of the inclusions. The massive collision of the inclusions not only accelerates the oxidation and coalescence of the impurities, but also assists the evaporation of the inclusions.

Based on the above results, here we propose three steps of oxygen-induced inclusions edulcoration in the formation of FMGs: i) Oxides, coming from the oxidation reaction between impurity elements and oxygen, nucleate and grow quickly. This stage is mainly controlled by the concentration of oxygen and the impurity elements. ii) Large inclusions form via random collision and coalescing of oxides, as well as adsorbing surrounding ions. When growing large enough, the movement of inclusions follows Stokes' Law [33] in the turbulent fluid. iii) Buoyancy rising, bubble attachment, and fluid flow transport large inclusions from the melt bulk to the top slag or to the refractory walls of the vessel. Details of these steps are illustrated as follow.

According to Kubaschewski [34], compared with the Fe, P and C, the Al, Si, S, etc. inclusions have stronger affinities with oxygen in the system (Ca>Al>Si>C>P). The reaction between these inclusions (Ca, Al, Si, etc.) and oxygen is more thermodynamically favored compared to the reaction between oxygen and the other elements in the system. Around the interface between oxygen and Fe, FeO is firstly generated but then diffuse into the liquid metal, followed by the oxidation of inclusions (Al, Cr, Si, S, and carbides) to form Al_2O_3, Cr_2O_3, SiO_2 particles and SO_2, CO gases [35], as Equation (1) shows.

$$x[M] + yFeO = M_xO_y + yFe \quad (1)$$

The adequate oxygen content promotes the oxidation of the impurity elements and increases the amount of oxides. From the homogeneous nucleation theory, the oxide embryos nucleate only when the oxides saturate in the liquid. Hence, a large number of oxides are unavoidably formed via the chemical reaction between the impurity elements and oxygen when blowing oxygen in the melt as shown in Fig. 10 (a). As the dissolved oxygen concentration is extremely low in the melt protected by argon, rare oxides are formed in the Ar-rod as shown in Fig. 10 (d).

With the increasing heating time, lots of oxide embryos in the O_2 blew melts collide with each other and coalesce into bigger ones as shown in Fig. 2 (f). Owing to the weak wettability of oxides during the solidification process, the oxides particles would not only be inclined to agglomerate together but also adsorb the surrounding S, Ca or other atoms to form larger inclusions rapidly and become more buoyant. These behaviors are chemically evidenced by first-principles calculations. Owing to the strong electronic hybridizations, O and Al, on the surface of α-Al_2O_3 favorably traps the free Ca and Si atoms and bond them with S and O to nucleate the CaS and SiO_2 clusters, respectively. As shown in Fig. 12 (a), the trapped Ca atom is tightly bounded to the nearest neighboring O and S atoms through the Ca-S and Ca-O bonding. The adsorption energy of the CaS-like clusters is −2.74 eV. Similarly, the trapped Si atom is tightly bounded to the nearest neighboring O atoms through the Si-O bonding and the trapped O atom is tightly bounded to the nearest neighboring Al atom through the Al-O bonding as shown in Fig. 12 (b). The adsorption energy of the SiO-like clusters is −8.40 eV. Containing more oxygen and oxides embryos, most inclusions in the oxygen blew melts thus encounter fast particle growth, whereas the growth of inclusions in the argon blew melts is not stimulated. This conclusion can be verified in Fig. 10, where inclusions in O_2-rod are much larger than those in Ar-rod when the holding time is long enough.

According to the Stokes law [33], the oxides inclusions would be inclined to agglomerate together and grow rapidly in the melts. The size of the inclusions has been theoretically calculated from the Stokes Law, as shown in Eq. (2),

$$r = \frac{r^*}{1 - \frac{g\alpha(\rho_m - \rho_s)r^*t}{18\eta_m}} \quad (2)$$

where r is the radius of inclusion; r^* is the initial radius of inclusion nucleus; α is the volume percentage of inclusion in the melt; g is gravity; ρ_m is the density of melt; ρ_s is the density of inclusions; η_m is the viscosity of melt. The radius of inclusions after collision and coalescing in the melt is related to the initial scale of inclusions, as well as the heating time. With $\rho_m = 7100$ kg/m^3, $\rho_s = 3000$ kg/m^3, $\eta_m = 0.005$ Pa s, $\alpha = 0.18$, we obtained the plot of the final size of inclusions with different initial scales vs. heating time, as shown in Fig. 13 (a). The inclusions with bigger nucleus size experience faster

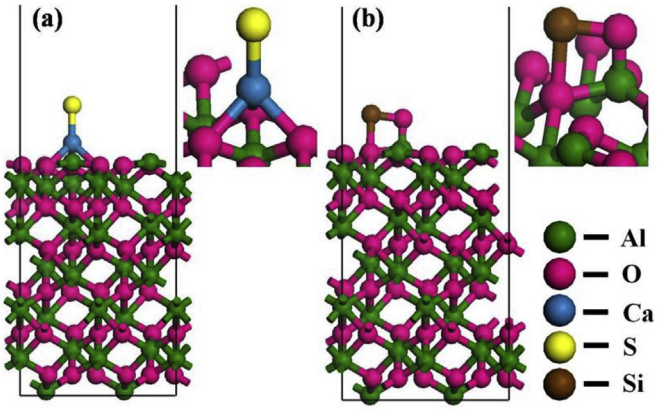

Fig. 12. First principles calculations of the adsorption behavior. (a) Nucleating process of CaS clusters by trapping S and Ca atoms on the Al_2O_3 (0001) surface. (b) Nucleating process of SiO_2 clusters by trapping Si and O atoms on the Al_2O_3 (0001) surface.

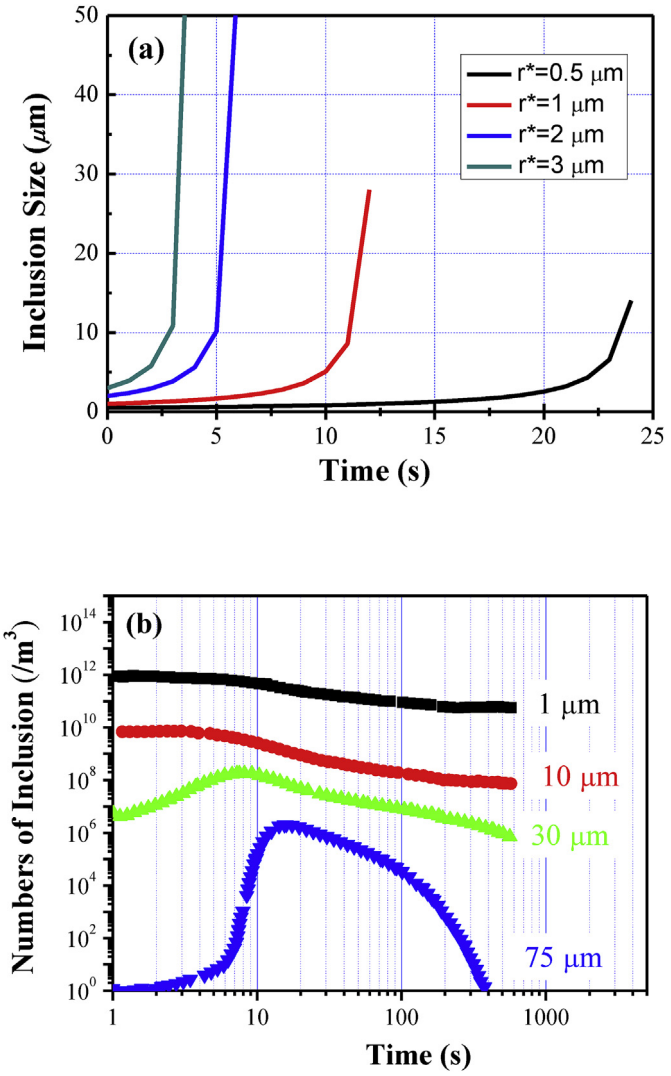

Fig. 13. (a) The relationship between radius of inclusions and holding time from theoretical arithmetic. (b) The number density change of inclusions with different scales with holing time.

particle growth than the smaller ones. The floating velocity of particles in fluids is proportional to the square of their diameters, which means that the bigger inclusions have higher rising velocities to float onto the free surface quickly. Based on the Stokes Law, the change rate of inclusion number density in melts can be obtained as the following equation [33]:

$$\frac{dn(r)}{dt} = \frac{1}{2}\int_0^r n(r_i)\alpha\lambda\beta(r_i,r_j)n(r_j)\left(\frac{r}{r_j}\right)^2 dr_i - n(r)\int_0^{r_{max}} n(r_j)\alpha\lambda\beta(r_i,r_j)dr_j - \frac{n(r)v}{H} - Mr^2n(r) \quad (3)$$

where $n(r)$ is the inclusion number density; λ is the effective collision coefficient of inclusion; r_i, r_j are the radius of inclusion i, j respectively (m); M is the constant for the calculation of adhesion of inclusion to the solid surfaces; $\beta(r_i,r_j)$ is the collision rate constant of r_i and r_j inclusions (m^3/s). With Eq. (3), we plotted the density change rate of inclusions with different radius, as shown in Fig. 13 (b). From the plot, larger inclusions may succeed to escape from the melts after a period of time, while the smaller ones are trapped in the melts eternally. Similar result was obtained for metallurgy research recently, the oxide inclusions with diameters >30 μm are able to float onto the top of the melts rapidly and their influences on the solidified melts easily vanish [32], while the oxides with diameters <30 μm float weakly and slowly to drift with the current of the thermosolutal convection from flotation-driven purification theory [33], and finally to be captured in the cooled solids. The oxygen blew into the melt also helps to mix the melt well to accelerate the oxidization and evaporation of inclusions. The inclusions in the melt can be oxidized by oxygen, and then the oxides and oxide-based inclusions evaporate out of the melt, which purifies the metallic melt. The typical preparation methods of glassy alloys, e.g. melt spinning, copper mold casting etc., are fast casting processes, similar as metallurgical casting, only with high cooling speed. As the inclusions in the O_2 blew melts are much larger than those in the argon blew melts, they can float out of the melts much easier and faster. As a result, the O_2-rods have rough surface but homogeneous interior, while the Ar-rods have smooth surface but inclusions spreading all over the interior, as Fig. 2 shows.

From the above analyses, the inclusions formed in the melts are made of oxides mostly, including Al_2O_3, CaS, SiO_2, P_2O_5, FeO, etc. However, only CaS and Al_2O_3 can survive as solid particles in the melts due to their high melting points. These particles serve as heterogeneous nucleation sites during solidification and significantly deteriorate the GFA of the obtained alloys. From Bramfitt's planar lattice disregistry model [36], the lattice of these oxides matches well with α-Fe [37], thus the oxides would decrease the interfacial energy for α-Fe precipitation. Trapping more inclusions inside the obtained rods, the samples prepared in argon are more likely enduring phase transformation from the amorphous state to the α-Fe phase with relatively short-range atomic diffusion. XRD results of samples annealed at 720 K and 750 K in Fig. 14 reveal the primary phases of Ar-rod and O_2-rod are α-Fe, Fe_3(P,C) and $Fe_{23}C_6$, respectively. The $Fe_{23}C_6$ phase possesses a lattice parameter larger than 1 nm including 116 atoms [38], drastically retarding its formation upon solidification due to the difficulty of the geometrical rearrangements in the relatively long-range ordering structures. Although the crystallization peaks of O_2-rod is splitted in Fig. 1 (b), the complicated atomic structure of its primary phase $Fe_{23}C_6$ requires higher energy for O_2-rod to crystallize. This explains why the O_2-rod present larger GFA than the Ar-rod. Furthermore, the

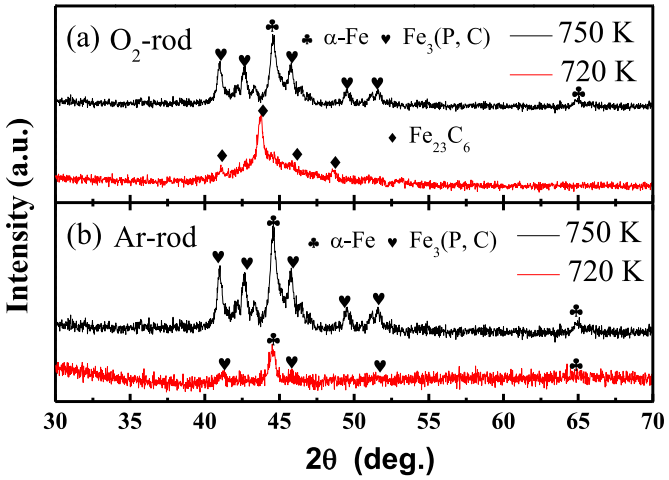

Fig. 14. XRD traces of $Fe_{80}P_{13}C_7$ glassy rods prepared using commercial raw materials under high purity oxygen (a) and argon (b) atmosphere annealed at 720 K and 750 K, respectively.

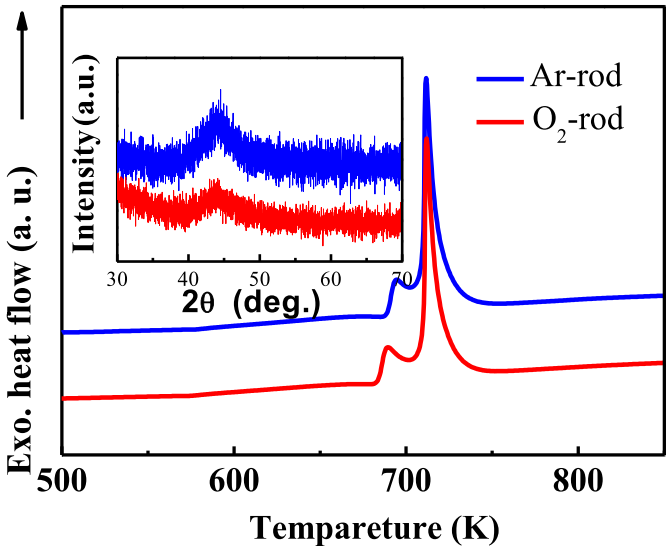

Fig. 15. XRD and DSC traces of $Fe_{80}P_{13}C_7$ glassy rods prepared using high-purity starting materials in argon and oxygen atmosphere.

magnetic and mechanical properties of BMGs also strongly depend on the type and amount of inclusions. The existence of the oxide inclusions in the FMGs should reduce their average magnetization and resist shear [17,30,39]. Thus, the enhancements of saturation magnetization and ductility of glassy rods prepared in oxygen probably result from a reduction of the inclusions formed in the FMGs.

To further verify our discoveries, 2.0 mm rods were prepared using high-purity starting materials in argon and oxygen atmosphere respectively. XRD analyses confirm the fully glassy structure of both samples. For high-purity starting materials, DSC analyses find no appreciable difference in T_g, T_x, or crystallization process in the samples prepared in argon or oxygen atmosphere (Fig. 15), which is consist with previous results by W. H. Wang et al. [22]. Without presence of the impurity elements, blowing oxygen doesn't facilitate the improvement of the GFA of the samples compared to blowing argon. It provides supportive evidence for the results that oxygen is the scavenger of inclusions in the formation of FMGs and the controllable blowing oxygen process is a very promising approach to reduce the industrial production cost of FMGs.

5. Conclusions

This work demonstrates that oxygen acts as “impurity-scavenger” during the preparation of FMGs, which means that the high-quality FMGs can be prepared using commercial raw materials by blowing oxygen. High-purity starting materials or high vacuum degree is not necessary for FMGs production. This discovery will for sure reduce the industrial production cost and promote the capacity of commercial production for FMGs greatly. Just as the oxygen top blown converter steelmaking brought the revolution of steel industry, this work not only provides an important insight into the understanding of the oxygen effect on glass formation, but also gives a useful guideline in the innovation of fabrication process for the industrial production of FMGs. However, there are still some critical issues need to be explored, for example, the composition of the inclusions depends on time, temperature and flow rate of oxygen. How to control the inclusions quantificationally? To address these issues, more refined scrutiny of experimental data is desired in future work.

Acknowledgments

This work was supported by the National Natural Science Foundation of China (No. 51871237 and 51631003), the Fundamental Research Funds for the Central Universities (No. 2015XKZD02), the Xuzhou Key Research & Development Program (KC17015), and the China Postdoctoral Science Foundation (2018T110569 and 2018M630623). The co-workers also thank the National Natural Science Foundation of China (No. 51501037 and 51561028).

References

[1] Q. Yu, X.D. Wang, H.B. Lou, Q.P. Cao, J.Z. Jiang, Atomic packing in Fe-based metallic glasses, Acta Mater. 102 (2016) 116–124.
[2] P. Duwez, S.C.H. Lin, Amorphous ferromagnetic phase in iron-carbon-phosphorus alloys, J. Appl. Phys. 38 (10) (1967) 4096–4097.
[3] J. Dai, Y.G. Wang, L. Yang, G.T. Xia, Q.S. Zeng, H.B. Lou, Structural aspects of magnetic softening in Fe-based metallic glass during annealing, Scr. Mater. 127 (2017) 88–91.
[4] J.Q. Wang, Y.H. Liu, M.W. Chen, G.Q. Xie, D.V. Louzguine-Luzgin, A. Inoue, J.H. Perepezko, Rapid degradation of azo dye by Fe-based metallic glass powder, Adv. Funct. Mater. 22 (12) (2012) 2567–2570.
[5] S. Pang, T. Zhang, K. Asami, A. Inoue, Synthesis of Fe-Cr-Mo-C-B-P bulk metallic glasses with high corrosion resistance, Acta Mater. 50 (3) (2002) 489–497.
[6] W. Yang, H. Liu, Y. Zhao, A. Inoue, K. Jiang, J. Huo, H. Ling, Q. Li, B. Shen, Mechanical properties and structural features of novel Fe-based bulk metallic glasses with unprecedented plasticity, Sci. Rep. 4 (2014) 6233.
[7] J.E. Gao, Z.P. Chen, Q. Du, H.X. Li, Y. Wu, H. Wang, X.J. Liu, Z.P. Lu, Fe-based bulk metallic glass composites without any metalloid elements, Acta Mater. 61 (9) (2013) 3214–3223.
[8] A. Inoue, Y. Shinohara, J.S. Gook, Thermal and magnetic properties of bulk Fe-based glassy alloys prepared by copper mold casting, Mater. Trans. JIM 36 (12) (1995) 1427–1433.
[9] Z. Lu, C. Liu, J. Thompson, W. Porter, Structural amorphous steels, Phys. Rev. Lett. 92 (24) (2004), 245503.
[10] S.D. Zhang, J. Wu, W.B. Qi, J.Q. Wang, Effect of porosity defects on the long-term corrosion behaviour of Fe-based amorphous alloy coated mild steel, Corrosion Sci. 110 (2016) 57–70.
[11] M. Fujikura, H. Sawairi, T. Sato, Influence of Sn addition on the magnetic properties of amorphous Fe-Si-B alloys containing Ti, J. Magn. Magn. Mater. 160 (1996) 289–290.
[12] H.X. Li, J.E. Gao, S.L. Wang, S. Yi, Z.P. Lu, Formation, crystallization behavior, and soft magnetic properties of FeCSiBP bulk metallic glass fabricated using industrial raw materials, Metall. Mater. Trans. A 43 (8) (2011) 2615–2619.
[13] X.H. Lin, W.L. Johnson, W.K. Rhim, Effect of oxygen impurity on crystallization of an undercooled bulk glass forming Zr-Ti-Cu-Ni-Al alloy, Mater. Trans. JIM 38 (5) (1997) 473–477.
[14] B.S. Murty, D.H. Ping, K. Hono, A. Inoue, Influence of oxygen on the crystallization behavior of $Zr_{65}Cu_{27.5}Al_{7.5}$ and $Zr_{66.7}Cu_{33.3}$ metallic glasses, Acta Mater. 48 (15) (2000) 3985–3996.
[15] J.L. Cheng, G. Chen, C.T. Liu, Y. Li, Innovative approach to the design of low-cost Zr-based BMG composites with good glass formation, Sci. Rep. 3 (2013) 2097.
[16] C.T. Liu, M.F. Chisholm, M.K. Miller, Oxygen impurity and microalloying effect in a Zr-based bulk metallic glass alloy, Intermetallics 10 (11) (2002) 1105–1112.
[17] R.D. Conner, R.E. Maire, W.L. Johnson, Effect of oxygen concentration upon the ductility of amorphous $Zr_{57}Nb_5Al_{10}Cu_{15.4}Ni_{12.6}$, Mater. Sci. Eng. A 419 (1–2) (2006) 148–152.
[18] A. Gebert, J. Eckert, L. Schultz, Effect of oxygen on phase formation and thermal stability of slowly cooled $Zr_{65}Al_{7.5}Cu_{17.5}Ni_{10}$ metallic glass, Acta Mater. 46 (15) (1998) 5475–5482.
[19] D.J. Sordelet, X.Y. Yang, E.A. Rozhkova, M.F. Besser, M.J. Kramer, Oxygen-stabilized glass formation in $Zr_{80}Pt_{20}$ melt-spun ribbons, Appl. Phys. Lett. 83 (1) (2003) 69.
[20] H.X. Li, J.E. Gao, Z.B. Jiao, Y. Wu, Z.P. Lu, Glass-forming ability enhanced by proper additions of oxygen in a Fe-based bulk metallic glass, Appl. Phys. Lett. 95 (16) (2009) 161905.
[21] Y.X. Wang, H. Yang, G. Lim, Y. Li, Glass formation enhanced by oxygen in binary Zr-Cu system, Scr. Mater. 62 (9) (2010) 682–685.
[22] C. Chang, J. Zhang, B. Shen, W. Wang, A. Inoue, Pronounced enhancement of glass-forming ability of Fe-Si-B-P bulk metallic glass in oxygen atmosphere, J. Mater. Res. 29 (10) (2014) 1217–1222.
[23] J. Pan, Q. Chen, N. Li, L. Liu, Formation of centimeter Fe-based bulk metallic glasses in low vacuum environment, J. Alloys Compd. 463 (1–2) (2008) 246–249.
[24] V. Ponnambalam, S.J. Poon, G.J. Shiflet, Fe-Mn-Cr-Mo-(Y,Ln)-C-B (Ln = Lanthanides) bulk metallic glasses as formable amorphous steel alloys, J. Mater. Res. 19 (10) (2011) 3046–3052.

[25] Z.P. Lu, C.T. Liu, W.D. Porter, Role of yttrium in glass formation of Fe-based bulk metallic glasses, Appl. Phys. Lett. 83 (13) (2003) 2581.
[26] J. Heinrich, R. Busch, F. Müller, S. Grandthyll, S. Hüfner, Role of aluminum as an oxygen-scavenger in zirconium based bulk metallic glasses, Appl. Phys. Lett. 100 (7) (2012), 071909.
[27] J. Pang, A. Wang, S. Yue, F. Kong, K. Qiu, C. Chang, X. Wang, C.-T. Liu, Fluxing purification and its effect on magnetic properties of high-B_s FeBPSiC amorphous alloy, J. Magn. Magn. Mater. 433 (2017) 35–41.
[28] C. Chang, T. Kubota, A. Makino, A. Inoue, Synthesis of ferromagnetic Fe-based bulk glassy alloys in the Fe-Si-B-P-C system, J. Alloys Compd. 473 (1–2) (2009) 368–372.
[29] A. Makino, X. Li, K. Yubuta, C. Chang, T. Kubota, A. Inoue, The effect of Cu on the plasticity of Fe-Si-B-P-based bulk metallic glass, Scr. Mater. 60 (5) (2009) 277–280.
[30] D. Granata, E. Fischer, V. Wessels, J.F. Löffler, Fluxing of Pd-Si-Cu bulk metallic glass and the role of cooling rate and purification, Acta Mater. 71 (2014) 145–152.
[31] T.D. Shen, R.B. Schwarz, Bulk ferromagnetic glasses prepared by flux melting and water quenching, Appl. Phys. Lett. 75 (1) (1999) 49.
[32] D. Li, X.Q. Chen, P. Fu, X. Ma, H. Liu, Y. Chen, Y. Cao, Y. Luan, Y. Li, Inclusion flotation-driven channel segregation in solidifying steels, Nat. Commun. 5 (2014) 5572.
[33] L. Zhang, S. Taniguchi, K. Cai, Fluid flow and inclusion removal in continuous casting tundish, Metall. Mater. Trans. B 31 (2) (2000) 253–266.
[34] O. Kubaschewski, C. Alcock, S.P.J. B, Materials Thermo-chemistry, sixth ed., Pergamon, New York, 1993, pp. 321–323.
[35] F. Oeters, Metallurgy of Steelmaking, Verlag Stahleisen, 1994.
[36] B.L. Bramfitt, The effect of carbide and nitride additions on the heterogeneous nucleation behavior of liquid iron, Metall. Trans. 1 (7) (1970) 1987–1995.
[37] H.X. Li, Z.P. Lu, S. Yi, Estimation of the glass forming ability of the Fe-based bulk metallic glass $Fe_{68.8}C_{7.0}Si_{3.5}B_{5.0}P_{9.6}Cr_{2.1}Mo_{2.0}Al_{2.0}$ that contains non-metallic inclusions, Met. Mater. Int. 15 (1) (2009) 7–14.
[38] M. Imafuku, S. Sato, H. Koshiba, E. Matsubara, A. Inoue, Crystallization behavior of amorphous $Fe_{90-X}Nb_{10}B_X$ (X = 10 and 38) alloys, Mater. Trans. JIM 41 (11) (2000) 1526–1529.
[39] T. Bitoh, D. Shibata, Constant permeability of $(Fe_{0.75}B_{0.20}Si_{0.05})_{96}Nb_4$ bulk metallic glass prepared by B_2O_3 flux melting and Cu-mold casting, J. Appl. Phys. 105 (7) (2009), 07A312.